

Electronic Supporting Information for

Diverse Chiral Assemblies of Nanoparticles Directed by Achiral Block Copolymers *via* Nanochannel Confinement

Qian Zhang, Jiabin Gu, Liangshun Zhang, and Jiaping Lin**

Shanghai Key Laboratory of Advanced Polymeric Materials, State Key Laboratory of Bioreactor Engineering, Key Laboratory for Ultrafine Materials of Ministry of Education, School of Materials Science and Engineering, East China University of Science and Technology, Shanghai 200237, China.

*Corresponding Author E-mail: zhangls@ecust.edu.cn (Zhang L.); jlin@ecust.edu.cn (Lin J.)

Contents

Part I. Self-Assembled Nanostructures of Confined Block Copolymers

Part II. Self-Assembled Nanostructures under Lower Loading of Nanoparticles

Part III. Three-Dimensional View of Self-Assembled Nanostructures

Part IV. Effects of Computational Parameters on CD Spectra

Part V. CD Spectra of Nanoparticle Assemblies

Part VI. CD Spectra of Defective Nanoparticle Assemblies

Part VII. CD Spectra of Decomposed Nanoparticle Assemblies

Part VIII. Effects of Physiochemical Properties of Nanoparticles

Part IX. Details of Hybrid Particle-Field Model

Part X. Details of Discrete Dipole Approximation

Part I. Self-Assembled Nanostructures of Confined Block Copolymers

For the cylinder-forming copolymers in bulk, the incorporation of nanochannel confinement encourages the formation of novel nanostructures (*i.e.*, single cylinder, stacked disk, single helix and double helix), which originate from the alleviation of entropy penalty of chain stretching. Fig. S1a summarizes the self-assembled nanostructures of block copolymers confined in nanochannels under various radii R_W . For the sake of clarity, the A-rich domains and part of the nanochannels are displayed in the top and side views. These nanostructures are in good agreement with the computational results reported by Li and co-workers.^{S1} By calculating the dimensionless free energy as a function of the nanochannel length, the relative stability and the corresponding phase diagram of these nanostructures are distinguished. Herein, we take the helical structures (including single and double helices) as examples. Fig. S1b displays the dimensionless free energy F of single and double helices as a function of the nanochannel length under the nanochannel radius $R_W = 4.0R_g$. The dimensionless free energy of helical structures in terms of the nanochannel length shows harmonic-like behaviors. The dotted and dashed lines highlight the lowest free energies F_{\min} of single and double helices at the nanochannel radius $R_W = 4.0R_g$, respectively. Fig. S1c plots the lowest free energies F_{\min} of single and double helices as a function of nanochannel radius R_W . The stable regions of single and double helices are identified, as illustrated by the dashed line.

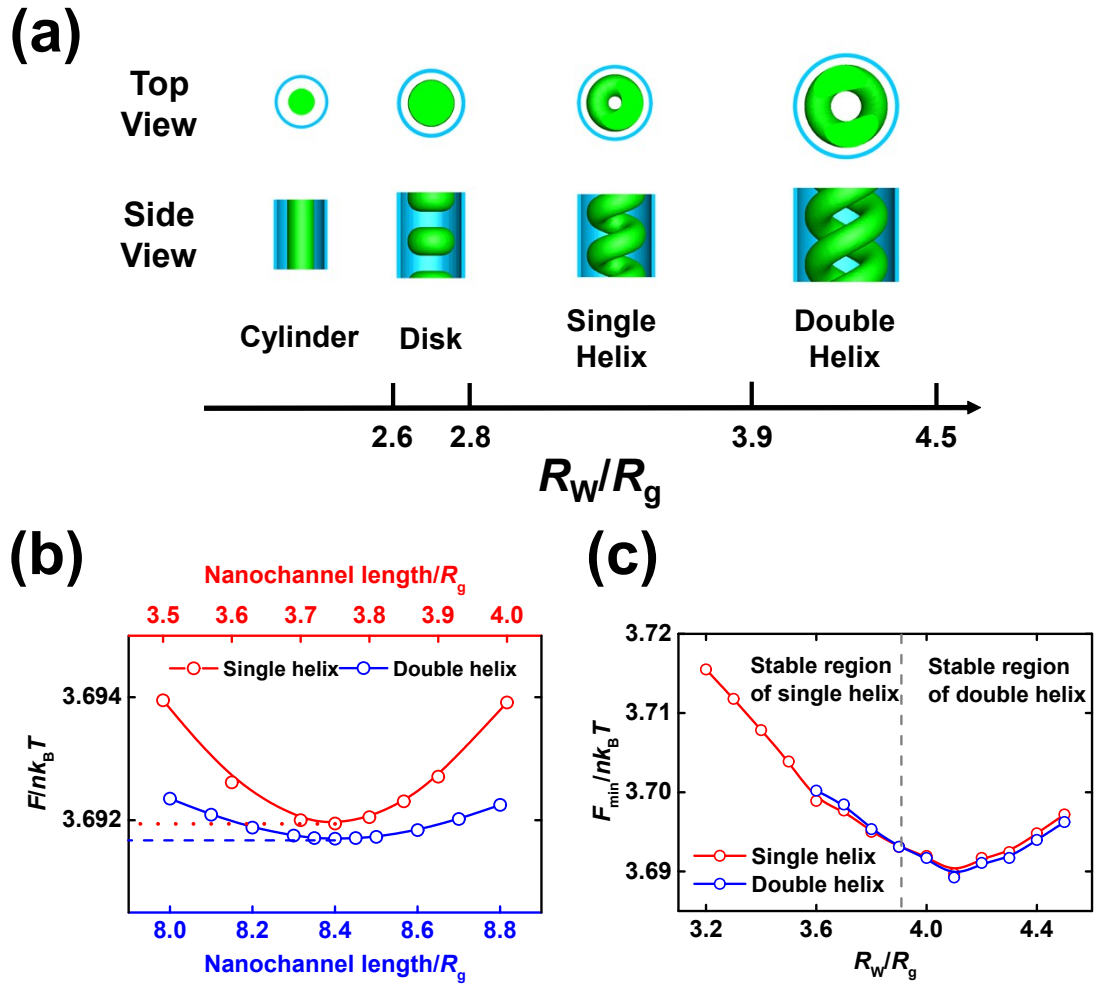


Fig. S1 (a) (Top and side views) Self-assembled nanostructures of block copolymers confined in nanochannels. The green and blue colors denote the A-rich domains and nanochannels, respectively. Parts of the nanochannels and the A-rich domains are displayed for clarify. (Bottom panel) Phase diagram of self-assembled nanostructures in terms of the nanochannel radius R_W . (b) Free energy comparisons of single and double helices as a function of the nanochannel length under the nanochannel radius $R_W = 4.0R_g$. The dotted and dashed lines highlight the lowest free energies F_{\min} of single and double helices, respectively. (c) The lowest free energies F_{\min} of single and double helices as a function of the nanochannel radius R_W . The dashed line indicates the case of nanochannel radius R_W , where $F_{\min}(\text{single helix}) = F_{\min}(\text{double helix})$ is satisfied.

Part II. Self-Assembled Nanostructures under Lower Loading of Nanoparticles

Under the condition of lower loading of nanoparticles, the interparticle interactions are weak, and the self-assembled nanostructures of block copolymers serve as scaffolds to program the spatial distribution of nanoparticles. As a result, the organization of nanoparticles closely resembles the self-assembled nanostructures of confined block copolymers, which are demonstrated in Fig. S2.

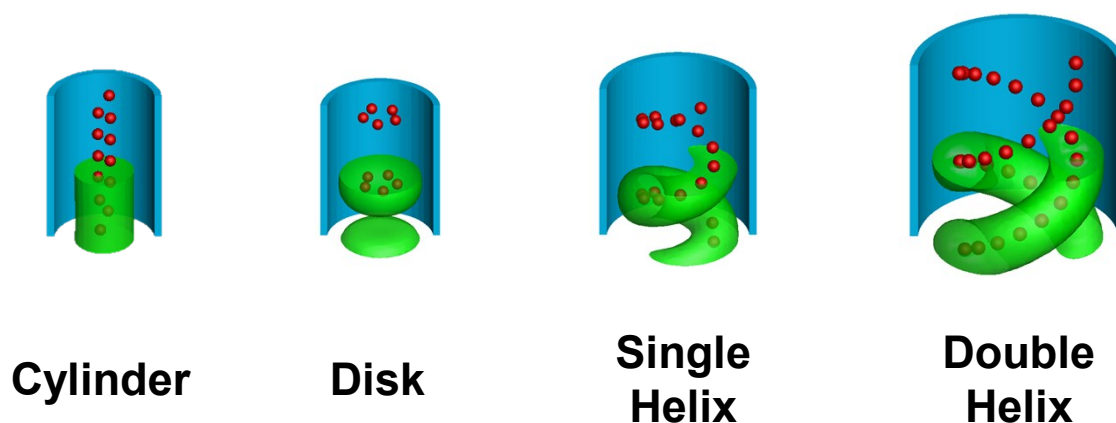
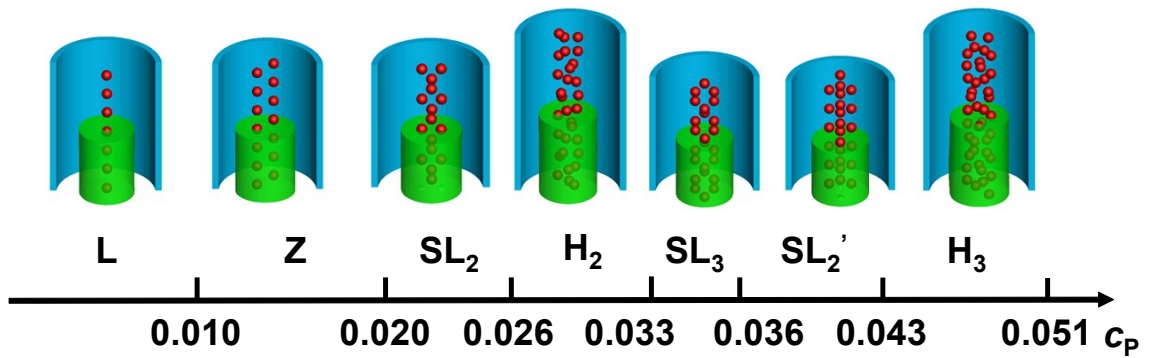


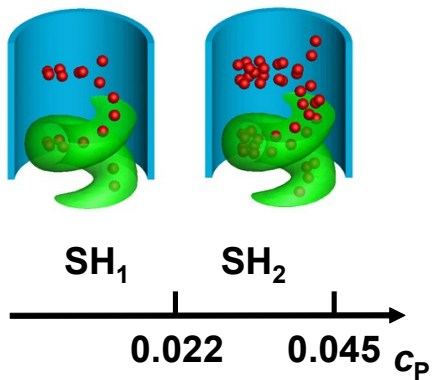
Fig. S2 Three-dimensional view of self-assembled nanostructures under various nanochannel radii $R_w = 2.6R_g$ (single cylinder), $2.7R_g$ (stacked disk), $3.2R_g$ (single helix), and $4.1R_g$ (double helix). The nanoparticle loading is fixed at $c_p = 0.019$. The red, green, and blue colors denote the nanoparticles, A-rich domains, and nanochannels, respectively. Parts of the nanochannel and the A-rich domains are displayed for clarify.

Part III. Three-Dimensional View of Self-Assembled Nanostructures

(a)



(b)



(c)

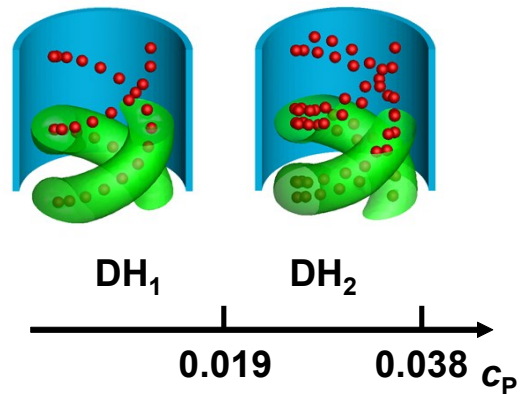


Fig. S3 Three-dimensional view of nanoparticle assemblies and corresponding phase diagram in terms of the nanoparticle loading c_p for various nanochannel radii $R_W =$ (a) $2.6R_g$, (b) $3.2R_g$ and (c) $4.1R_g$. The red, green, and blue colors denote the nanoparticles, A-rich domains, and nanochannels, respectively. Parts of the nanochannel and the A-rich domains are displayed for clarify. The other representations are the same as those in Fig. 2 of main text.

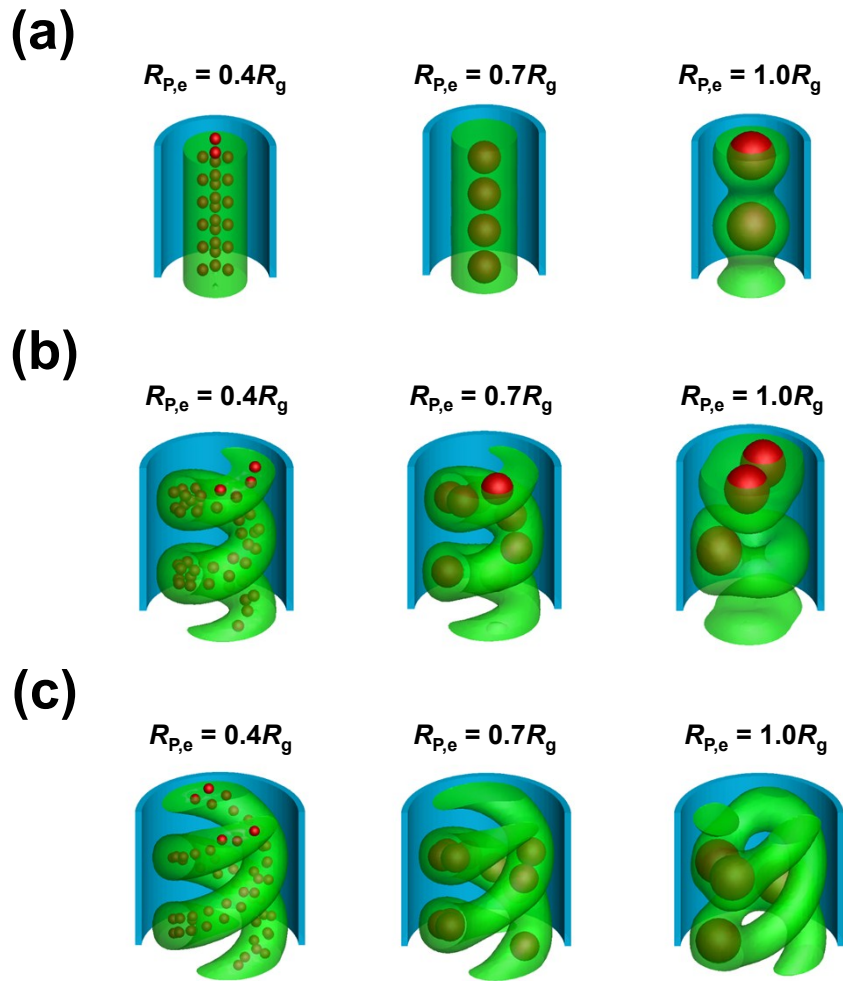


Fig. S4 Effect of effective nanoparticle radius $R_{p,e}$ on the morphologies of self-assembled nanostructures of block copolymer/nanoparticle composites. The parameter settings of nanochannel radius R_W and nanoparticle loading c_p are: (a) $R_W = 2.6R_g$ and $c_p = 0.040$, (b) $R_W = 3.2R_g$ and $c_p = 0.045$, and (c) $R_W = 4.1R_g$ and $c_p = 0.038$.

Part IV. Effects of Computational Parameters on CD Spectra

In the main text, we focus on the CD spectra of nanoparticle assemblies embedded in background medium of water. Herein, we also calculate the CD spectra of nanoparticle assemblies embedded in background medium of block copolymers, which have refractive index of $n = 1.600$. The single helices of nanoparticles formed at nanochannel radius $R_w = 3.2R_g$ are taken as examples. The morphologies of single helices of nanoparticles can be referred to Fig. 2 in the main text. As shown in Fig. S5, the CD spectra of nanoparticle assemblies embedded in different mediums exhibit similar bisignated shape, and the strength of CD responses of nanoparticle assemblies is dependent upon the nanoparticle loading. However, an increase of the refractive index leads to red shifts of CD bands and enhancements of CD signals.

In the DDA simulations, the calculated extinction and CD spectra are sensitive to the discretization degree and the replica number of nanoparticle assemblies. To ensure the numerical convergence of DDA simulations, the effects of discretization parameter (SHPAR1) on the extinction and CD spectra are investigated. The SHPAR1 parameter controls the discretization degree of target object. A larger value of SHPAR1 indicates a larger dipole number N_d and thus smaller dipole spacing d . The previous studies of Draine and co-workers suggest that the criterion of $2\pi|m|d/\lambda < 1$ should be satisfied to achieve numerical convergence of simulated spectra,^{S2} where m is the complex refractive index of target material. Fig. S6a, b and c displays the convergence test of extinction and CD spectra for the H_2 , SH_1 and DH_1 assemblies at wavelength of 540 nm, respectively. With an increase of SHPAR1, a good convergence of extinction and CD spectra is identified. In our DDA calculations, the parameter settings of SHPAR1 for the nanochannel radii $R_w = 2.6R_g$, $3.2R_g$ and $4.1R_g$ are chosen as 60, 100 and 120, respectively. These parameter settings of SHPAR1 lead to the values of dipole

spacing of 0.36 nm ($R_W = 2.6R_g$), 0.46 nm ($R_W = 3.2R_g$) and 0.47 nm ($R_W = 4.1R_g$). Therefore, the criterion of $2\pi|m|d/\lambda < 1$ can be satisfied within the wavelength range studied here (400 nm $< \lambda < 800$ nm).

In the DDA simulations, the input configuration of nanoparticle assemblies (*i.e.*, H_n , SH_n and DH_n assemblies) is the replicas of single-periodic assemblies obtained from the HPF model. To ensure the numerical convergence of DDA results, the effect of replica number n_{replica} on the normalized CD spectra is investigated. Fig. S7 illustrates the convergence of CD spectra with respect to the replica number n_{replica} of SH_1 assembly. It can be found that the CD spectra become convergent with an increase of n_{replica} . In our DDA simulations, the input configurations of H_n , SH_n , DH_n assemblies are two-, five-, and three-fold duplicates (*i.e.*, $n_{\text{replica}} = 2, 5, \text{ and } 3$) of configurations obtained from the HPF model.

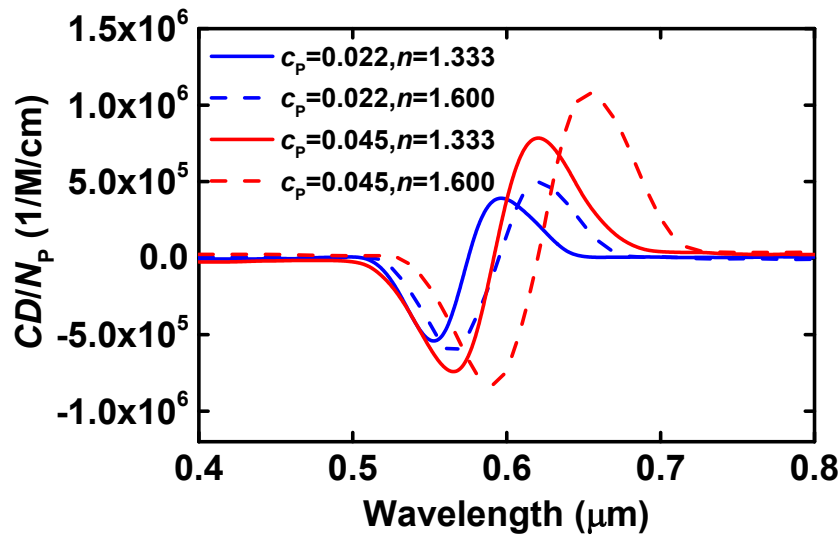


Fig. S5 Effect of the refractive index of background medium on the CD spectra of nanoparticle assemblies. The nanochannel radius is set as $R_W = 3.2R_g$.

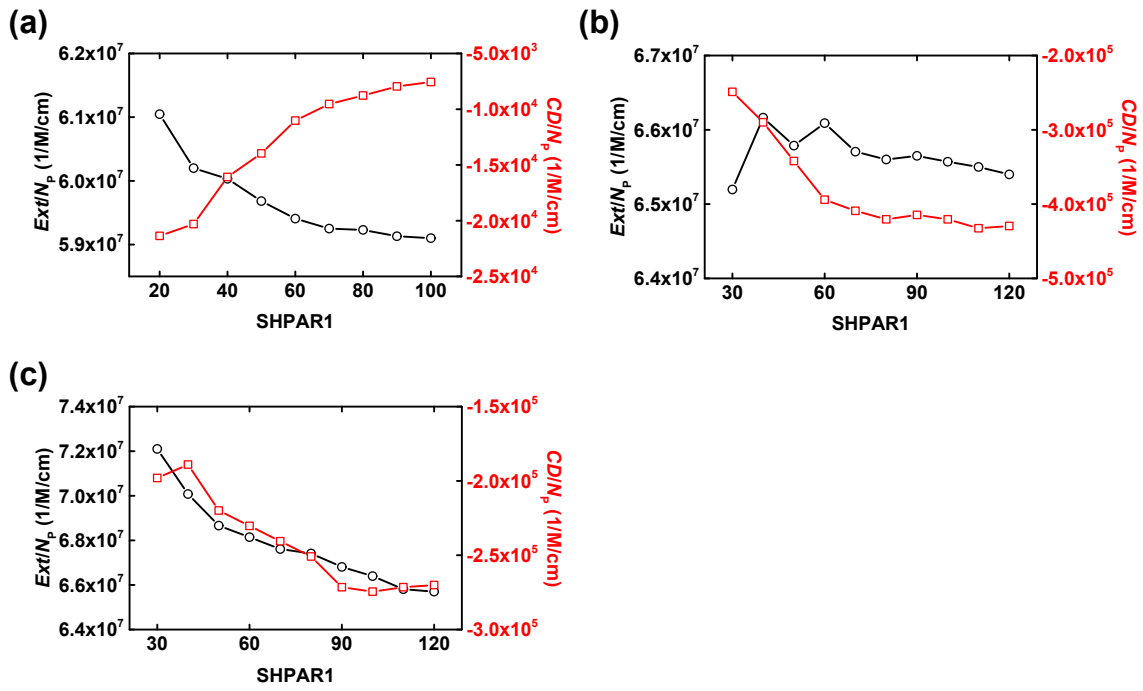


Fig. S6 Influence of discretization parameter SHPAR1 on the extinction and CD spectra at wavelength of 540 nm for the (a) H_2 , (b) SH_1 and (c) DH_1 assemblies of nanoparticles.

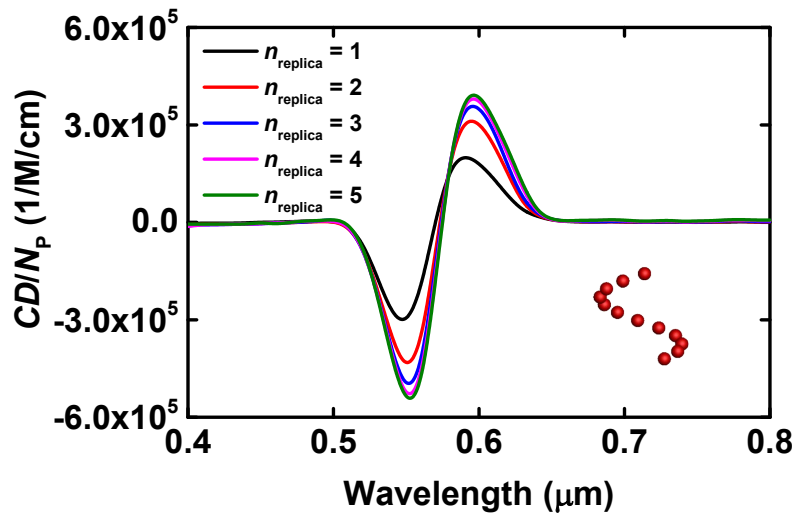


Fig. S7 Influence of replica number n_{replica} on the normalized CD of SH_1 assembly. The inset shows the structural details of SH_1 assembly from the HPF model (*i.e.*, $n_{\text{replica}}=1$).

Part V. CD Spectra of Nanoparticle Assemblies

In main text, we focus on the CD behaviors of nanoparticle assemblies at the nanochannel radii of $R_W = 3.2R_g$ and $4.1R_g$. Herein, the CD behaviors of nanoparticle assemblies under the condition of nanochannel radius $R_W = 2.6R_g$ are discussed. Fig. S8 illustrates the geometrical representations (top panel) and the simulated CD spectra (bottom panel) of staggered layers of nanoparticles (including SL_2 , SL_3 , and SL_2') and the three-stranded helices (H_3). In comparison with the cases of SH_n and DH_n assemblies (Fig. 4 in main text), the CD spectra of SL_n and H_3 assemblies exhibit weak intensity and asymmetry shape. The weak CD responses of SL_n assemblies can be attributed to the achiral arrangement of nanoparticles, which is characterized by the near-zero values of chiral order parameter (Fig. 3 in the main text).

For the H_3 assembly with nonzero value of chiral order parameter, its weak CD responses can be explained in terms of the degeneracy of handedness. The CD responses of H_2 assembly have similar features. As illustrated in Fig. S9a and b, the H_2 and H_3 assemblies can be decomposed into both right- and left-handed twists. The degeneracy of right- and left-handed configurations weakens the preferential attenuation of circularly polarized lights, leading to weak CD responses.

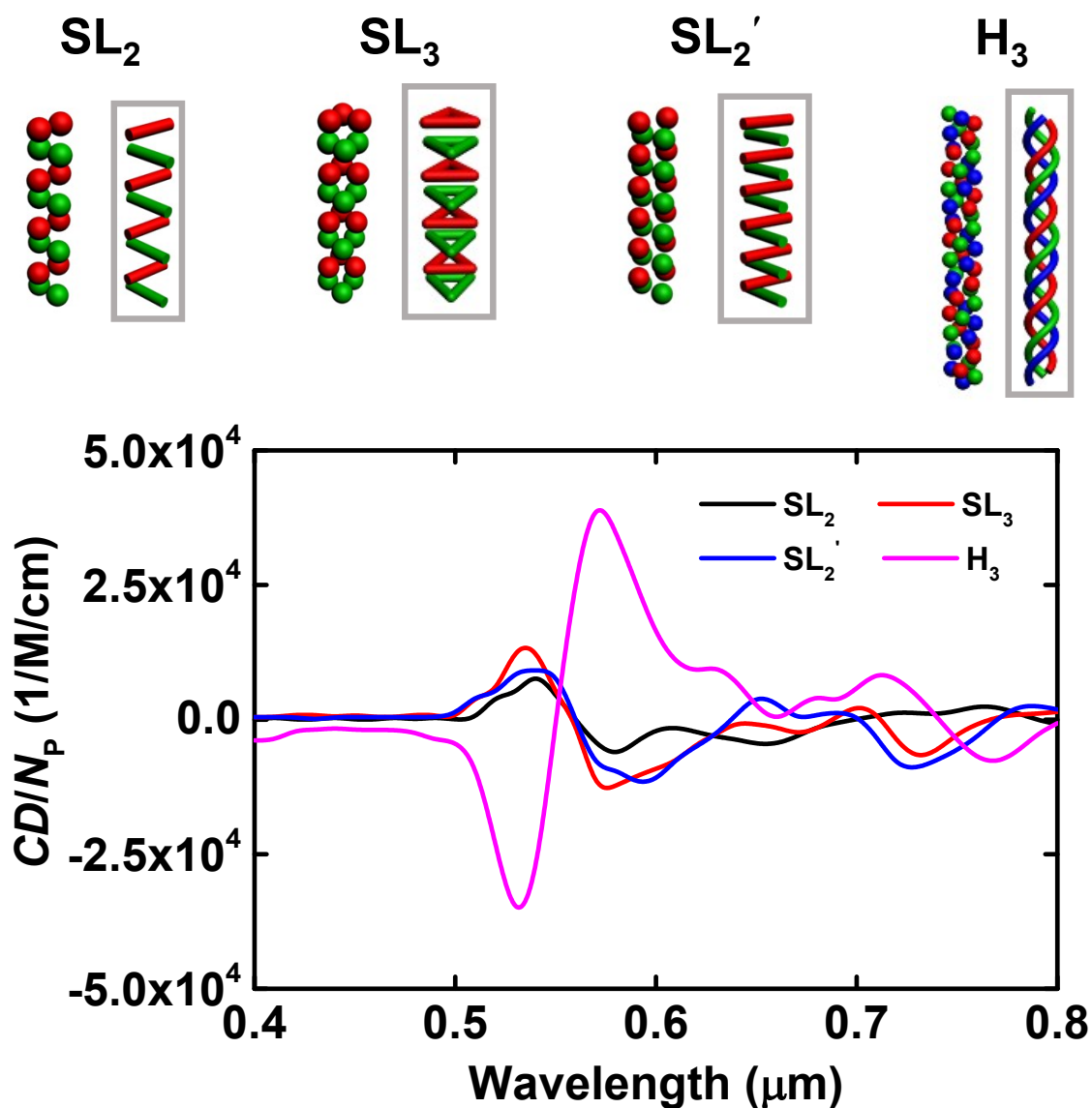


Fig. S8 (Top panel) Nanoparticle assemblies and their geometrical representations enclosed in rectangles. The nanoparticle assemblies are designated as SL_n for staggered layers with n nanoparticles and H_n for multi-stranded helices with n spirals. The nanoparticles belonging to different layers or spirals are labeled by distinct colors for clarity. (Bottom panel) Simulated CD spectra of nanoparticle assemblies. The nanoparticle loadings are $c_p = 0.025$ (SL_2), $c_p = 0.035$ (SL_3), $c_p = 0.038$ (SL_2') and $c_p = 0.044$ (H_3).

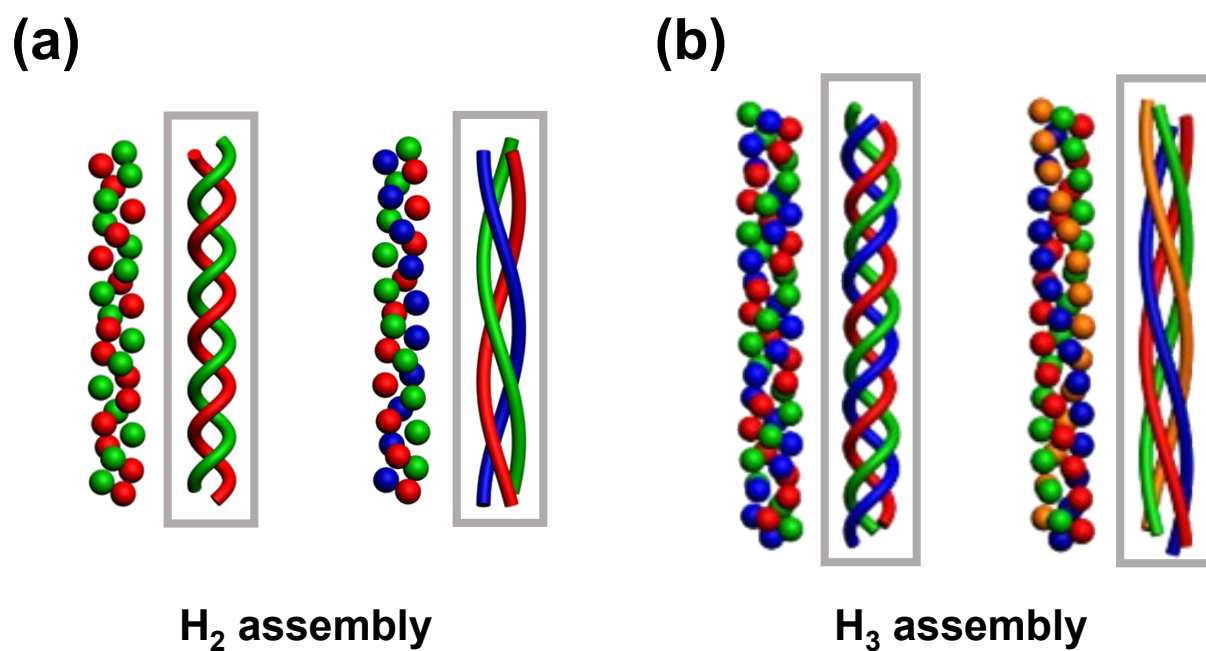


Fig. S9 Illustration of the degeneracy of handedness for (a) H₂ and (b) H₃ assemblies. The geometrical representations are enclosed in the rectangles. The nanoparticles belonging to different spirals are labeled by distinct colors for clarity.

Part VI. CD Spectra of Defective Nanoparticle Assemblies

For the nanochannel radius $R_W = 3.2R_g$, the defective double-layered single helices (SH_2) of nanoparticles are observed in the region of $0.022 < c_p < 0.045$. To investigate the influence of defects on the CD behaviors of SH_2 assemblies, the CD spectra of defective SH_2 assemblies are calculated and plotted in Fig. S10. The defective SH_2 assemblies exhibit characteristic bisignate dip-peak CD signals. As c_p is increased, the enhancement of CD strength and the red shifts of CD bands are observed.

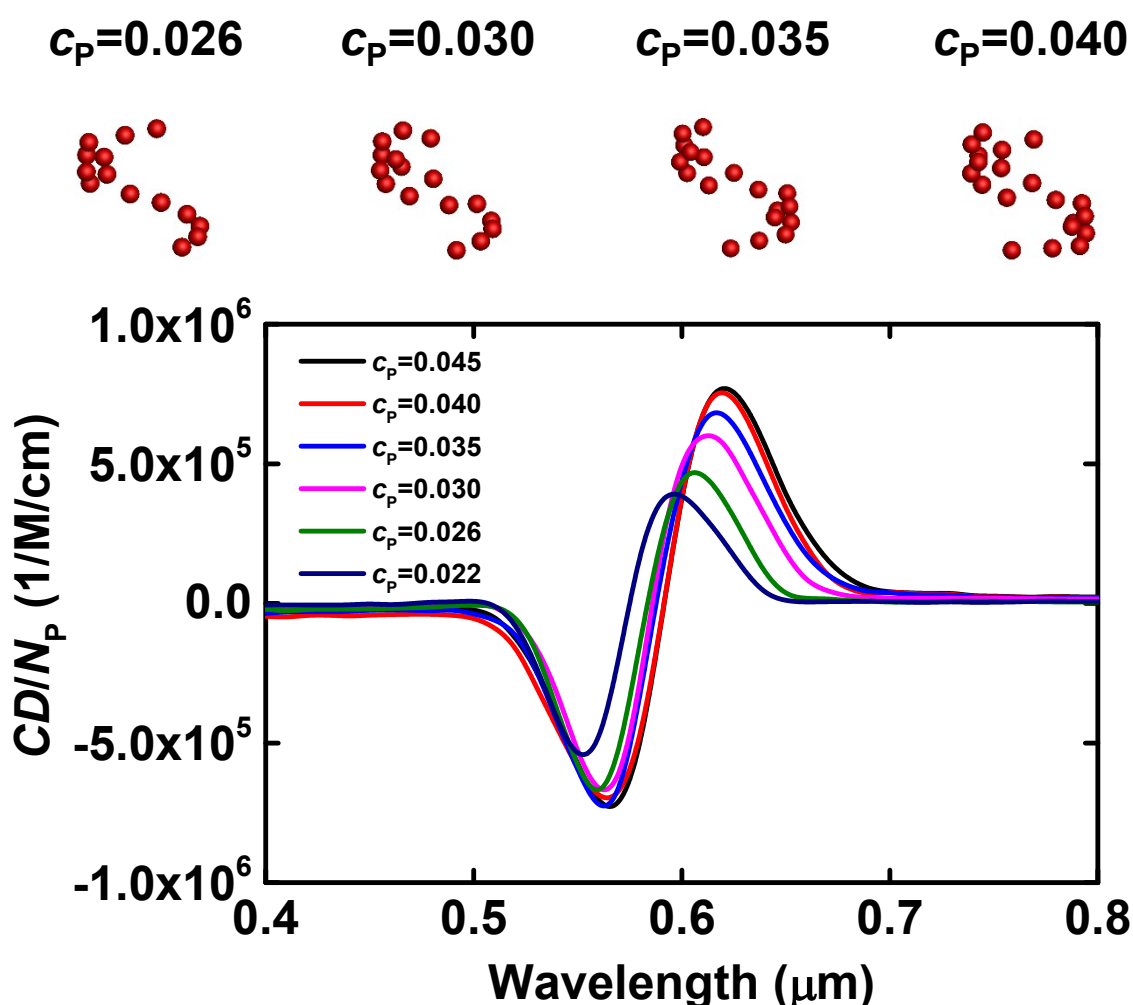


Fig. S10 (Top panel) Structural details and (bottom panel) simulated CD spectra of SH_n assemblies for nanochannel radius $R_W = 3.2R_g$. The nanoparticle loading c_p is tuned from 0.022 to 0.045.

Part VII. CD Spectra of Decomposed Nanoparticle Assemblies

The DH_n assemblies are composed of two isolated strands. Herein, we decompose the DH_1 assembly (under the conditions of nanochannel radius $R_W = 4.1R_g$ and nanoparticle loading $c_P = 0.019$) into two isolated strands $1/2DH_1$ and $(1/2DH_1)'$, as illustrated in the top panel of Fig. S11. The CD spectra of these two isolated strands are calculated and plotted in the bottom panel Fig. S11. The CD spectra of isolated strands are very close to that of primary DH_1 assembly, indicating that the inter-helix interactions of nanoparticles in the DH_n assemblies are negligible.

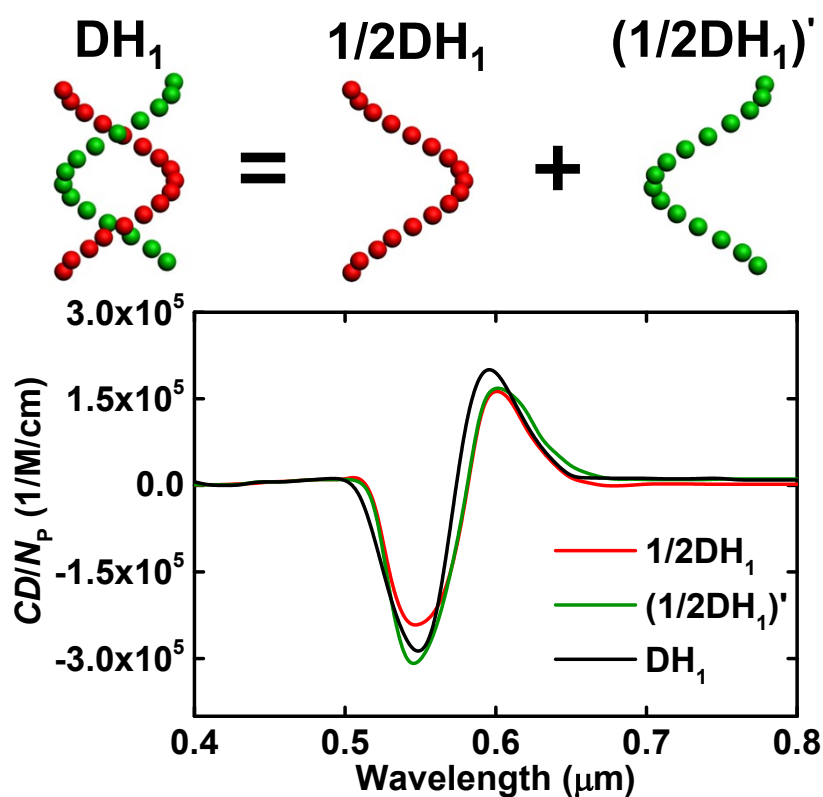


Fig. S11 (Top panel) Illustration for the decomposition of primary DH_1 assembly into isolated $1/2DH_1$ and $(1/2DH_1)'$ strands. The primary DH_1 assembly is formed under the conditions of nanochannel radius $R_W = 4.1R_g$ and the nanoparticle loading $c_P = 0.019$. The nanoparticles belonging to different strands are labeled by distinct colors for clarity. (Bottom panel) The simulated CD spectra of isolated $1/2DH_1$ and $(1/2DH_1)'$ strands as well as primary DH_1 assembly.

Part VIII. Effects of Physiochemical Properties of Nanoparticles

Herein, we examine the effect of effective nanoparticle radius $R_{p,e}$ on the SH₁ assembly in the case of nanochannel radius $R_W = 3.2R_g$. As shown in Fig. S12a, the SH₁ assemblies of nanoparticles with effective radius of $R_{p,e} = 0.3R_g$ are found in range of $c_p < 0.009$, which is narrower than the case of nanoparticles with effective radius of $R_{p,e} = 0.4R_g$ (Fig. 2b). Moreover, with a decrease of nanoparticle radius, the CD strength of SH₁ assembly becomes weaker and the CD bands are blue-shifted (Fig. S12b), which are in consistent with previous experimental observations.^{S3}

In addition to the radius of nanoparticles, the range of interparticle repulsion (described by cutoff radius r_C in Lennard-Jones potential of Equation S4) is another variable to affect the assemblies of nanoparticles. In the main text, the cutoff radius r_C of interparticle repulsion is set as $r_C = 0.15R_g$. Herein, we examine the influences of cutoff radius r_C on the SH₁ assembly in the case of nanochannel radius $R_W = 3.2R_g$. As shown in Fig. S13, the nanoparticles with large cutoff radius ($r_C = 0.45R_g$) can form loosely packed SH₁ assembly exhibiting weak CD strength.

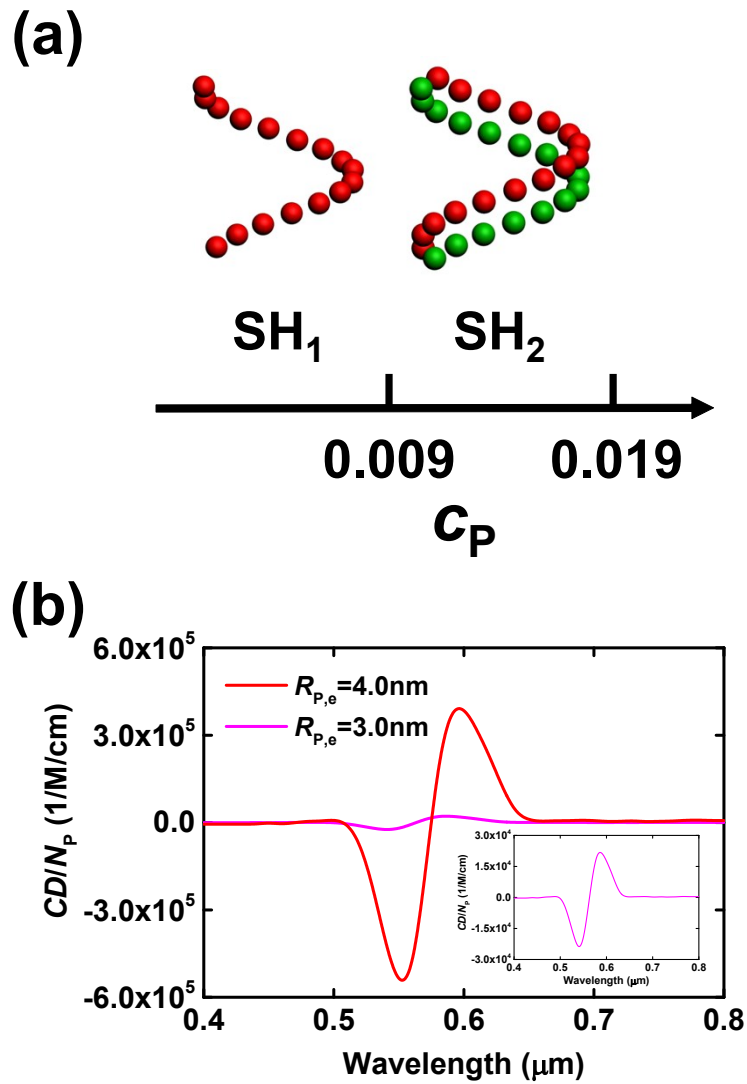


Fig. S12 (a) Nanoparticle assemblies and corresponding phase diagram in terms of the nanoparticle loading c_P for effective nanoparticle radius $R_{p,e} = 0.3R_g$. (b) Simulated CD spectra of SH₁ assemblies for various effective nanoparticle radii $R_{p,e}$. The inset illustrates the CD spectrum for the case of $R_{p,e} = 3.0 \text{ nm}$. The nanochannel radius is fixed at $R_W = 3.2R_g$.

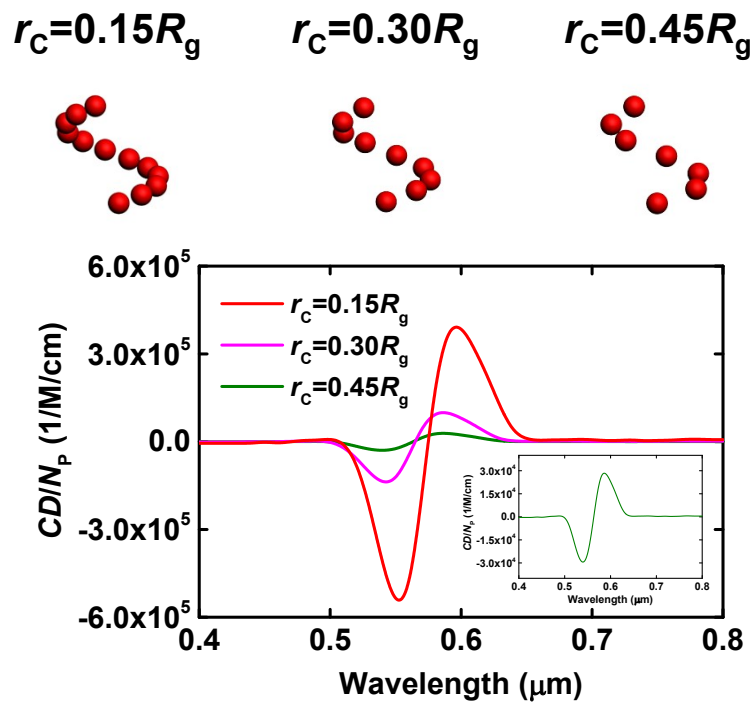


Fig. S13 (Top panel) Illustrations of SH₁ assemblies of nanoparticles with various cutoff radii. (Bottom panel) Simulated CD spectra of SH₁ assemblies of nanoparticles with various cutoff radii. The inset illustrates the CD spectrum for the case of $r_c = 0.45R_g$. The effective radius of nanoparticles is fixed at $R_{P,e} = 0.4R_g$ (4.0 nm), and the nanochannel radius is set as $R_W = 3.2R_g$.

Part IX. Details of Hybrid Particle-Field Model

In the hybrid particle-field (HPF) model, the nanocomposite system with volume of V is confined in a nanochannel. The nanocomposite consists of n monodisperse AB block copolymers and n_p nanoparticles, which are illustrated in Fig. 1a of main text. The achiral block copolymers are modeled as the Gaussian chains with the gyration radius of $R_g = b(N/6)^{1/2}$, where N is the segment number of a single chain and b is the statistical segment length. The composition of A blocks in polymer chains is denoted by f_A . The i -th nanoparticle with coordinate of \mathbf{r}_i is represented by a cavity function

$$h_i(r) = 0.5 \times \left[1 - \tanh \left(\frac{|r - r_i| - R_{P,e}}{\gamma} \right) \right] \quad (\text{S1})$$

where $R_{P,e}$ defines the effective radius of nanoparticle and γ describes the width of particle-

polymer interface. The local volume fraction of nanoparticles is given by $\varphi_p(r) = \sum_{i=1}^{n_p} h_i(r)$.

The nanoparticle loading in the nanocomposite is determined by $c_p = V_p/V$, where $V_p = \int d\mathbf{r} \varphi_p(\mathbf{r})$ denotes the total volume of nanoparticles. The nanochannel confinement is introduced by 'masking' technique,^{S4,S5,S6} in which the nanochannel is modeled as a local volume fraction field given by

$$\varphi_w(r) = \tanh \left(\frac{d(r) - R_w}{I_w} \right) \quad (\text{S2})$$

where $d(\mathbf{r})$ represents the distance from position \mathbf{r} to nanochannel axis, R_w defines the nanochannel radius and I_w characterizes the width of nanochannel-polymer interface.

The free energy functional (in units of $k_B T$) of nanocomposite system has the following form

$$F = U_{PP} + U_{AB} - TS \quad (\text{S3})$$

In this expression, U_{PP} denotes the interparticle interactions given by

$$U_{PP} = \sum_{i=1}^{n_P-1} \sum_{j>i}^{n_P} \int dr' h_i(r') \int dr h_j(r) u(|r' - r|) \quad (\text{S4})$$

where $u(r)$ represents the repulsive part of Lennard-Jones potential. The second and third terms of Equation S3 describe the energy contributions from the interactions among the block copolymers, the nanoparticles and the nanochannel

$$U_{AB} - TS = n(1 - c_P) \ln \frac{V(1 - c_P)}{Q} + \frac{n}{V} \int dr \left\{ \frac{1}{2} \sum_{IJ} \chi_{IJ} N \varphi_I \varphi_J + \kappa \left(\sum_I \varphi_I - 1 \right) - \sum_K \omega_K \varphi_K \right\} \quad (\text{S5})$$

where φ_I (I, J = A, B, P and W) represents the local volume fraction of I-type component and ω_K (K = A and B) defines the potential field of K-type component. χ_{IJ} denotes the Flory-Huggins interaction parameter between different components. The variable κ controls the incompressibility of system. Q is the normalized single-chain partition function for block copolymers. On the basis of field-theoretical framework of polymers, the self-consistent field equations are derived through minimization of free energy functional with respect to the variables ω_K and φ_K

$$\frac{\delta F}{\delta \omega_K} = 0 \quad (\text{S6})$$

$$\frac{\delta F}{\delta \varphi_K} = 0 \quad (\text{S7})$$

$$\frac{\delta F}{\delta \kappa} = 0 \quad (\text{S8})$$

In current model, only the spherical nanoparticles are considered. The motion of nanoparticles obeys the Newton's equations. The force \mathbf{F}_i exerted on the i -th nanoparticle is given by

$$\mathbf{F}_i = \int d\mathbf{r} \mathbf{f}_i(\mathbf{r}) \quad (\text{S9})$$

The body force $\mathbf{f}_i(\mathbf{r})$ has a formula

$$\mathbf{f}_i(\mathbf{r}) = h_i(\mathbf{r})(-\nabla\mu_i(\mathbf{r}) - \zeta\mathbf{v}_i - \nabla\eta) \quad (\text{S10})$$

where $\mu_i(\mathbf{r}) \equiv \delta F/\delta h_i(\mathbf{r})$ represents the chemical potential and \mathbf{v}_i denotes the velocity of i -th nanoparticle. ζ characterizes the Stokes friction coefficient and η implies the Gaussian white noise satisfying the fluctuation-dissipation theorem.

All the numerical calculations are implemented in the three-dimensional boxes with periodic boundary conditions on each direction. The box length in x - y plane is slightly larger than the nanochannel diameter, and the lattice spacing in x - y plane is fixed at $0.125R_g$ to ensure the numerical accuracy. For given nanochannel radius, a range of nanochannel lengths (*i.e.*, the length of simulation boxes in z direction) are tuned to minimize the dimensionless free energy of systems. The algorithm for solving the HPF equations can be referred to our previous work.^{S7}

In our calculations, the composition of block copolymers is fixed at $f_A = 0.26$ and the effective radius of nanoparticles is chosen as $R_{p,e} = 0.4R_g$. The widths of the particle-polymer and nanochannel-polymer interfaces are set as $\gamma = 0.125R_g$ and $I_W = 0.25R_g$, respectively. For each parameter setting, ten independent runs with different random seeds and initial configurations are implemented to ensure the reproducibility of calculated results.

In the experiments, the inorganic nanoparticles are usually functionalized by a rich variety of ligands such as oligomeric surfactants and grafted homopolymers.^{S8,S9,S10} The physico-chemical properties of ligand chains can be incorporated into the HPF model *via* the particle-polymer interface, which plays a critical role in the self-assembly of block copolymer-based nanocomposites. To demonstrate the validity of such treatment in the HPF model, we use the self-consistent field theory (SCFT) to describe the system of ligand-grafted (designated as L)

nanoparticle (P) immersed in a homopolymer matrix (A),^{S11} as illustrated in Fig. S14a. Herein, the core radius of nanoparticle is denoted by $R_{P,c}$. The interaction between the grafting ligands and the homopolymers is described by the combined Flory-Huggins interaction parameter $\chi_{AL}N$. The length ratio of homopolymers to ligands is denoted by α . The dimensionless grafting density of ligands is defined as $\sigma^* = \sigma \cdot R_g^2 / C$, where the grafting density σ is the number of ligands per unit surface area of grafted sphere and C is the dimensionless monomer density.

Figure S14b shows the local volume fractions ($\varphi_{P,c}$ and φ_L) of nanoparticle and ligands as a function of the radial coordinate r for the nanoparticle core radius $R_{P,c} = 0.275R_g$. Note that a narrower interface in the core of nanoparticle is introduced for numerical consideration. It is confirmed that the grafting ligands form a layer surrounding the core of nanoparticle. As a comparison, the summation of $\varphi_{P,c}$ and φ_L obtained from the SCFT as well as the cavity function of nanoparticles in the HPF model are also plotted in Fig. S14b. It can be seen that the summation of local volume fractions of nanoparticle and ligands obtained from the SCFT can be well reflected by the profiles of nanoparticles in the HPF model. Thus, the layer of grafting ligands can be simplified as the nanoparticle-polymer interfacial region surrounding the nanoparticle.

The width γ of particle-polymer interface is impacted by the grafting density σ^* , the grafting ligand-homopolymer interaction parameter $\chi_{AL}N$ and the length ratio α of homopolymers to ligands, which are depicted in Fig. S14c and d. Note that the parameter setting of γ (*i.e.*, $\gamma = 0.125R_g$) is highlighted by the dashed lines. For given value of σ^* , it is found that an increase of $\chi_{AL}N$ or α results in a thin ligand layer, corresponding to a decrease of γ . In addition, a threefold increase of γ can be achieved with an increase of σ^* from 0.12 to 0.36. The

calculation results are generally consistent with the theoretical predictions and experimental observations of Composto and co-workers.^{S12,S13}

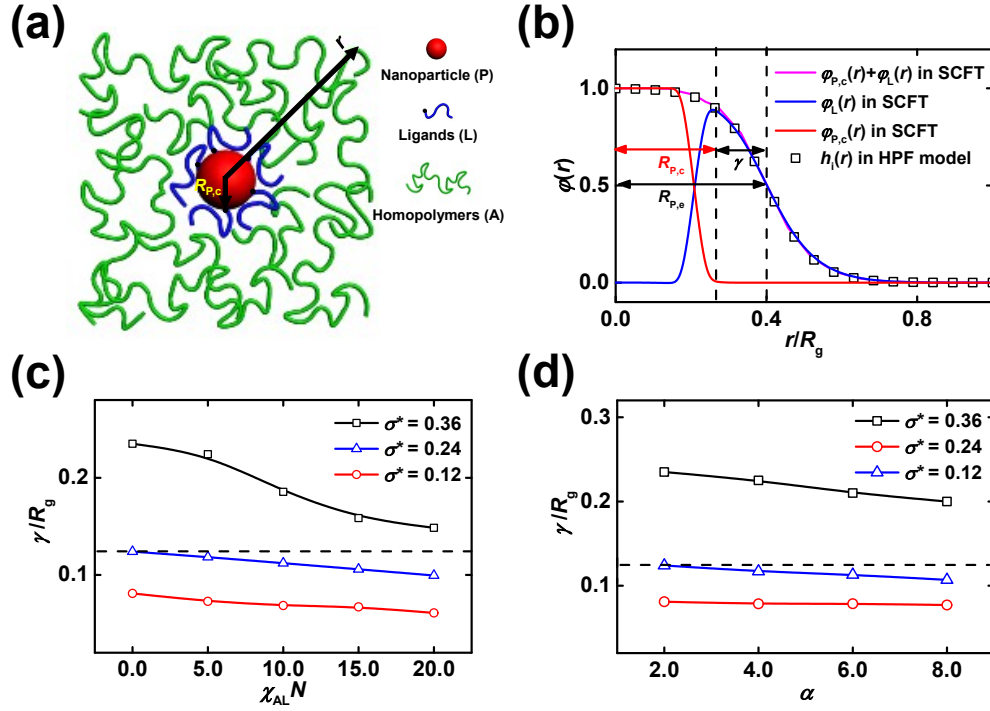


Fig. S14 (a) Schematic illustration of the geometry of ligand-grafted (designated as L) nanoparticle (P) immersed in a homopolymer matrix (A). $R_{P,c}$ denotes the core radius of nanoparticle. (b) Local volume fractions ($\phi_{P,c}$, ϕ_L and $\phi_{P,c} + \phi_L$) of nanoparticles, ligands and their summation along the radial direction of nanoparticle obtained from the self-consistent field theory (SCFT). The squares represent the local volume fraction of nanoparticles in the hybrid particle-field (HPF) model. The parameter settings of grafting density σ^* , interaction parameter $\chi_{AL}N$ and length ratio α are: $\sigma^* = 0.24$, $\chi_{AL}N = 0.0$ and $\alpha = 2.0$. (c) Variation of particle-polymer interface width γ as a function of the interaction parameter $\chi_{AL}N$ between ligands and homopolymers under various grafting densities σ^* . The length ratio of homopolymers to ligands is fixed at $\alpha = 2.0$. (d) Variation of particle-polymer interface width γ as a function of the length ratio α . The interaction parameter is fixed at $\chi_{AL}N = 0.0$. In panels (c) and (d), the dashed lines highlight the value of $\gamma = 0.125R_g$, corresponding to the parameter setting of particle-polymer interface width γ .

Part X. Details of Discrete Dipole Approximation

The discrete dipole approximation (DDA) is a flexible and powerful technique to reproduce the essential optical properties of an object with arbitrary geometry.^{S14,S15,S16,S17,S18} In DDA simulations, a target object is discretized into a finite array of N -point dipoles with polarizabilities α_i at position \mathbf{r}_i . The polarization of i -th dipole is

$$P_i = \alpha_i \left(E_{inc,i} - \sum_{i \neq j} E_{j \rightarrow i} \right) \quad (\text{S11})$$

where $\mathbf{E}_{inc,i} = \mathbf{E}_0 \exp(i\mathbf{k} \cdot \mathbf{r}_i - i\omega t)$ denotes the electric field of incident wave. $\mathbf{E}_{j \rightarrow i}$ represents the field induced by the j -th dipole written as

$$E_{j \rightarrow i} = \frac{\exp(ikr_{ij})}{r_{ij}^3} \left\{ k^2 r_{ij} \times (r_{ij} \times P_j) + \frac{1 - ikr_{ij}}{r_{ij}^2} [r_{ij}^2 P_j - 3r_{ij}(r_{ij} \cdot P_j)] \right\} = A_{ij} \cdot P_j \quad (\text{S12})$$

where $k = 2\pi/\lambda$ denotes the wave number, $\mathbf{r}_{ij} = \mathbf{r}_i - \mathbf{r}_j$ and $r_{ij} = |\mathbf{r}_i - \mathbf{r}_j|$. \mathbf{A}_{ij} is a 3×3 matrix defining the contribution from the j -th dipole to the field at \mathbf{r}_i . On the basis of Equation S11 and S12, the final set of linear equations for the solution of \mathbf{P}_i is given by

$$E_{inc,i} = \frac{P_i}{\alpha_i} + \sum_{i \neq j} A_{ij} \cdot P_j \quad (\text{S13})$$

Once the polarizations \mathbf{P} are obtained, the extinction cross section for circularly polarized incident waves (\pm) is calculated as

$$\sigma_{ext,\pm} = \frac{4\pi k}{|E_{inc}|^2} \sum_{i=1} \text{Im}(E_{inc,i,\pm}^* \cdot P_{i,\pm}) \quad (\text{S14})$$

The extinction CD cross section is given by

$$\sigma_{ext,CD} = \langle \sigma_{ext,+} - \sigma_{ext,-} \rangle_{\Omega} \quad (\text{S15})$$

where $\langle \rangle_{\Omega}$ indicates the average over orientations. It should be mentioned that the quantity outputted by DDSCAT program is a series of efficiency factor such as the extinction efficiency factor $Q_{\text{ext}} = \sigma_{\text{ext}}/\pi a_{\text{eff}}^2$, where a_{eff} is the effective radius of a sphere with N -point dipoles. The normalized CD (*i.e.*, CD/N_{P}) in the convenient units $(\text{cm}\cdot\text{M})^{-1}$ presented here is calculated as $CD/N_{\text{P}} = \langle Q_{\text{ext},+} - Q_{\text{ext},-} \rangle_{\Omega} \times \pi a_{\text{eff}}^2/N_{\text{P}} \times (N_{\text{A}}/0.23) \times 10^{-4}$.

To calculate the CD spectra of the nanoparticle assemblies directed by the confined block copolymers, the coordinates of nanoparticles in our HPF simulations are served as the input configuration of DDSCAT program with target type of 'SPHERES_N', which is illustrated in Fig. 1b of main text. The nanoparticles are assumed to be gold (Au) nanoparticles with radius of 4.0 nm. The real and imaginary parts of dielectric constants of Au nanoparticles are obtained from the literature of Johnson and Christy.^{S19}

References

- S1 W. Li and R. A. Wickham, *Macromolecules*, 2006, **39**, 8492-8498.
- S2 B. T. Draine and J. Goodman, *Astrophys. J.*, 1993, **405**, 685-697.
- S3 A. Kuzyk, R. Schreiber, Z. Fan, G. Pardatscher, E.-M. Roller, A. Högele, F. C. Simmel, A. O. Govorov and T. Liedl, *Nature*, 2012, **483**, 311-314.
- S4 M. W. Masten, *J. Chem. Phys.*, 1997, **106**, 7781-7791.
- S5 V. Khanna, E. W. Cochran, A. Hexemer, G. E. Stein, G. H. Fredrickson, E. J. Kramer, X. Li, J. Wang and S. F. Hahn, *Macromolecules*, 2006, **39**, 9346-9356.
- S6 V. Mishra, S. Hur, E. W. Cochran, G. E. Stein, G. H. Fredrickson and E. J. Kramer, *Macromolecules*, 2010, **43**, 1942-1949.
- S7 Q. Zhang, L. Zhang and J. Lin, *J. Phys. Chem. C*, 2017, **121**, 23705-23715.
- S8 J. J. Chiu, B. J. Kim, E. J. Kramer and D. J. Pine, *J. Am. Chem. Soc.*, 2005, **127**, 5036-5037.
- S9 R. Mout, D. F. Moyano, S. Rana and V. M. Rotello, *Chem. Soc. Rev.*, 2012, **41**, 2539-2544.
- S10 C. Yi, S. Zhang, K. T. Webb and Z. Nie, *Acc. Chem. Res.*, 2017, **50**, 12-21.
- S11 T. L. Chantawansri, S.-M. Hur, C. J. García-Cervera, H. D. Ceniceros and G. H. Fredrickson, *J. Chem. Phys.*, 2011, **134**, 244905.
- S12 A. L. Frischknecht, M. J. A. Hore, J. Ford and R. J. Composto, *Macromolecules*, 2013, **46**, 2856-2869.
- S13 J. Choi, M. J. A. Hore, J. S. Meth, N. Clarke, K. I. Winey and R. J. Composto, *ACS Macro Lett.*, 2013, **2**, 485-490.

- S14 T. Jensen, L. Kelly, A. Lazarides and G. C. Schatz, *J. Cluster Sci.*, 1999, **10**, 295-317.
- S15 B. T. Draine and P. J. Flatau, *J. Opt. Soc. Am. A*, 1994, **11**, 1491-1499.
- S16 B. T. Draine, *Astrophys. J.*, 1988, **333**, 848-872.
- S17 B. T. Draine and P. J. Flatau, *J. Opt. Soc. Am. A*, 2008, **25**, 2693-2703.
- S18 P. J. Flatau and B. T. Draine, *Opt. Express*, 2012, **20**, 1247-1252.
- S19 P. B. Johnson and R. W. Christy, *Phys. Rev. B*, 1972, **6**, 4370-4379.